https://doi.org/10.1007/s41230-024-3068-z

GPa-level pressure-induced enhanced corrosion resistance in TiZrTaNbSn biomedical high-entropy alloy

Xiao-hong Wang[1], Yu-lei Deng[1], Qiao-yu Li[1], Zhi-xin Xu[1], *Teng-fei Ma[1], Xing Yang[1], **Duo Dong[2], Dong-dong Zhu[2], and Xiao-hong Yang[1]

1. Key Laboratory of Air-driven Equipment Technology of Zhejiang Province, Quzhou University, Quzhou 324000, Zhejiang, China

2. School of Materials Science and Engineering, Taizhou University, Taizhou 318000, Zhejiang, China

Abstract: TiZrTaNb-based high-entropy alloys (HEAs) are research frontier of biomedical materials due to their high hardness, good yield strength, excellent wear resistance and corrosion resistance. Sn, as an essential trace element in the human body that plays a significant role in physiological process. It has stable chemical properties and a low elastic modulus. In this study, a new material, TiZrTaNbSn HEAs, was proposed as a potential biomedical alloy. The $Ti_{35}Zr_{25}Ta_{15}Nb_{15}Sn_{10}$ biomedical high-entropy alloys (BHEAs) were successfully prepared through an arc melting furnace and then remelted using a German high-temperature and high-pressure apparatus under GPa-level (4 GPa and 7 GPa). The precipitation behavior of the needle-like HCP-Zr_5Sn_3 phase that precipitates discontinuously at the grain boundary was successfully controlled. The phase constitution, microstructure, and corrosion resistance of the alloy were studied. The results show that the needle-like HCP-Zr_5Sn_3 phase is eliminated and the (Zr, Sn)-rich nano-precipitated phase is precipitated in the microstructure under high pressure, which leads to the narrowing of grain boundaries and consequently improves the corrosion resistance of the alloy. In addition, the formation mechanisms of (Zr, Sn)-rich nanoprecipitates in BHEAs were discussed. More Zr and Sn dissolve in the matrix due to the effect of high pressure, during the cooling process, they precipitate to form a (Zr, Sn)-rich nano-precipitated phase.

Keywords: biomedical HEAs; precipitation; grain boundary; corrosion resistance; TiZrTaNbSn

CLC numbers: TG146.23 **Document code:** A **Article ID:** 1672-6421(2024)03-265-11

1 Introduction

Titanium alloys have attracted siginificant attention as biomedical materials in recent years due to their good mechanical properties and excellent physiological corrosion resistance [1-3]. However, the application of titanium biomedical materials has a limitation due to the biocompatibility and stress shielding [4]. To address this problem, researchers have developed β-Ti alloys. The elastic modulus of these alloys is relatively close to that of human bone [5, 6]. On this basis, the nontoxic β-Ti alloys are designed, which are expected to break through the shortage of materials used in traditional artificial joints in clinical applications. Previous studies have shown that when V, Ta, Nb, and Mo elements with the same crystal structure are added to Ti, it is prone to form an infinite solid solution [7-9]. Moreover, additions of Si, Cr, Mn, Fe, Co, Ni and Cu elements can form a eutectoid alloy with limited solid solution [10-12]. Furthermore, Zr and Sn are neutral addition element for β-Ti alloys [13, 14].

In 2004, Ye et al. [15-17] proposed a new concept for a high entropy alloy. The alloy generally contains 5 to 13 main elements, and the atomic proportion of each main element is between 5% and 35%. Impressively, it is easy to form simple solid solution phase with a high-configuration entropy [18]. Furthermore, it is found that the properties of some HEAs are much

***Teng-fei Ma**

Male, born in 1987, Ph. D. His research interests mainly focus on the lightweight high-strength structural material and advanced forming technology. He has presided and participated 10 provincial and ministerial projects, and published more than 50 papers.

E-mail: matengfeihit@163.com

****Duo Dong**

E-mail: dongduohit@163.com

Received: 2023-06-28; Accepted: 2024-01-30

better than those of traditional alloys in various aspects, including fracture resistance [19], tensile strength [20], corrosion resistance [21], and oxidation resistance [22]. Among them, Ti-Zr-based HEAs usually possess body centered cubic solid solution structures, and show relatively high hardness, yield strength and wear resistance [23, 24], and they are expected to serve as a stress-bearing implant material, which can resist plastic deformation and fracture under high stress conditions. In addition, the high wear resistance reduces the risk of inflammation after implantation into the human body [25-28]. In addition to good mechanical properties, it has been reported that the compositional elements of refractory HEAs, such as Ta, Nb, Mo, and Hf, can form a dense oxide film on the alloy surface to prevent the invasion of external anions, ensuring the good corrosion resistance of the alloy [29-31]. Wang et al. [27] studied the electrochemical behavior of the TiZrTaNbMo HEA in phosphate buffered solution (PBS). The research shows that the TiZrTaNbMo HEA exhibits good corrosion resistance, similar to the Ti6Al4V alloy, and its pitting resistance is significantly stronger than that of 316L stainless steel and the CoCrMo alloy. Moreover, Motallebzadeh et al. [28] found that the corrosion potential and current density obtained by TiZrTaNbHf and $Ti_{1.5}ZrTa_{0.5}Nb_{0.5}Hf_{0.5}$ in PBS solution are superior to those obtained by Ti6Al4V. Wang's latest research has shown that Nb and Ta alloying can reduce point defects in passivation films; TiZr(Nb, Ta) medium entropy alloys have higher corrosion resistance levels than pure titanium [32]. Good corrosion resistance can reduce the harm of metal ion dissolution to human health, thereby demonstrating good biocompatibility. As an essential trace element in the human body, Sn plays an important role in inhibiting the development of cancer cells, promoting metabolic growth, and facilitating wound healing [33].

In this work, a comprehensive consideration was given to both cytotoxic elements and β stable elements on bone homeostasis, Zr, Ta, Nb, and Sn four elements were selected to prepare Ti series biomedical high entropy alloys (BHEAs). However, when Hf, Mo, Zr, Nb, Ti, Cr, W and V elements are present in the alloy, in addition to BCC phase, a small amount of HCP phase is also found to exist within the material [32]. Depressingly, when the HCP phase precipitates discontinuously at the grain boundary and grows parallel to the grain in the form of a needle, it weakens the corrosion resistance of the alloy.

To control the phase transformation in the solidification process of metals or alloys, the traditional method involves adjusting the chemical composition and temperature. The pressure, which is another thermodynamic parameter that affects the solidification process, is usually ignored. Pressure, is also an important thermodynamic variable that has a significant impact on the solidification process of alloy [34-36]. Especially, when the pressure reaches GPa level, it greatly changes the thermodynamics and dynamics of metal or alloy solidification process [37-39]. The purpose of the present study is to evaluate a novel high-entropy alloy TiZrTaNbSn, which primarily consists of a BCC structure and a small amount of HCP. GPa-level pressure was used to regulate the precipitation and distribution of HCP phase to enhance the corrosion resistance of the alloy. The microstructure, crystal structure, corrosion resistance of TiZrTaNbSn obtained via conventional and high-pressure synthesis methods were investigated.

2 Experimental

2.1 Sample preparation

The raw materials of high-purity Ti, Zr, Ta, Nb, and Sn, from Beijing Dream Material Technology Co., Ltd., were mixed according to the nominal compositions of the $Ti_{35}Zr_{25}Ta_{15}Nb_{15}Sn_{10}$. The alloy master ingot with a total mass of 150 g was prepared in a vacuum arc melting furnace under a high purity argon atmosphere (99.9%) with a vacuum of 10^{-5} Pa. Before melting, the furnace chamber was washed with argon at least 3 times and the sponge Ti was put into one of the water-cooled crucible to absorb residual oxygen. All of these ingots were remelted at least five times to ensure a uniform distribution of the composition. All rods (Φ3 mm × 3.7 mm and Φ3 mm × 1 mm) were cut from the lower parts of the ingots by wire-cut electrical-discharge machining (WEDM). The specimen was polished after grinding with 180–2000 grit silicon carbide sandpaper.

The high pressure samples were prepared by a German Max Voggenreiter 6-8 walker high-temperature and high-pressure apparatus. The maximum pressure and temperature of the equipment were 25 GPa and 2,500 K, respectively. Before synthesis, the sample, the BN tube, graphite sheets, the graphite tube, Mo columns, and octahedral pyrophyllite were placed in a blast drying oven, and kept at 100 °C for 24 h. Then, the samples were assembled after drying according to Fig. 1. BN tubes were used as thermal insulation materials, graphite tubes acted as heating materials, and Mo columns played a role in heat conduction and support. At the beginning of the experiment, the pressure was slowly increased to 4 GPa/7 GPa within 3 h, and then the temperature was increased to 1,800 K at a rate of approximately 150 $K \cdot min^{-1}$. After holding the temperature for 10 min, the system was cooled to room temperature and the pressure was released. The solidification conditions were the same except for high pressure.

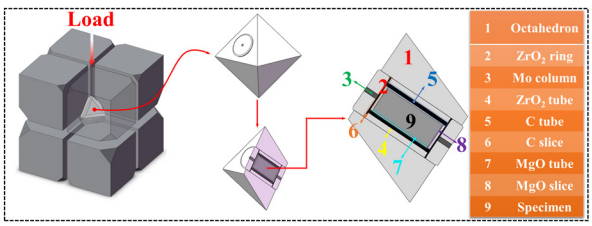

Fig. 1: Schematic diagram of high-pressure solidification experiment assembly

2.2 Structure characterization

A Rigaku Smartlab X-ray diffractometer (XRD) was used to characterize the crystal structure. The light source was monochromatic Cu target Kα-rays at 40 kV and 40 mA, the

scanning range 2θ was 30°–90°, and the scanning rate was 10°·min^{-1}. The morphologies of the samples were analyzed by a JSM-7001F scanning electron microscope (SEM). Moreover, the accompanying energy dispersive spectrometer (EDS) was used for compositional analysis. The TEM observations were performed in a TECNAI G2 F20 at 200 kV for the bright-field (BF) image, dark-field (DF) image, selected area electron diffraction (SAED), and high-resolution TEM (HRTEM) investigations.

2.3 Corrosion experiment

Electrochemical tests were performed on an electrochemical workstation (CHI660E) using a three-electrode-cell system. Firstly, samples with a size of Φ3 mm × 1 mm were embedded in an epoxy resin and connected to a copper wire as the working electrode. Then, the surface of samples was polished with silicon carbide sandpaper to 2000 grit, followed by ultrasonic cleaning in deionized water and ethanol. A platinum electrode was used as the counter electrode, and saturated mercuric chloride was used as the reference electrode. The test temperature was 25 °C, the scanning speed was 1 mV·s^{-1}, and the scanning voltage range was from –1.5 V to +1.5 V. Finally, alternating current impedance (AC impedance) was used to measure the polarization curve and eletrochemical impedance spectroscopy (EIS). The morphologies were examined by SEM, and the composition of the corroded surface was examined by EDS.

3 Results

3.1 Microstructure and phase constitution of $Ti_{35}Zr_{25}Ta_{15}Nb_{15}Sn_{10}$ BHEA samples after solidification at different pressures

The microstructure of the $Ti_{35}Zr_{25}Ta_{15}Nb_{15}Sn_{10}$ HEA solidified at different pressures is shown in Fig. 2. At ambient pressure (0.1 MPa), the alloy shows a typical equiaxed dendrite structure with obvious segregation, and there are obvious needle-like phases growing parallel to the matrix, and the grains are relatively coarse, as shown in Figs. 2(a) and (b). After solidification at 4 GPa, the precipitates growing in parallel between dendrites almost disappear, and precipitates are dispersed and uniformly distributed in the matrix. Subgrain boundaries begin to appear in the dendrites, and the grain size decreases compared to that at ambient pressure, as shown in Figs. 2(c) and (d). Furthermore, when the solidification pressure increases to 7 GPa, the average grain size further decreases, and the intragranular subgrain boundaries densify.

Figure 3 shows the backscattered electron morphology (BSE) and grain boundary spacing characteristics of the $Ti_{35}Zr_{25}Ta_{15}Nb_{15}Sn_{10}$ BHEAs after solidification at different pressures. The interdendritic width is approximately 7.67 μm at ambient pressure, which is 0.69 μm and 0.6 μm at 4 GPa and 7 GPa, decreasing by 91% and 92.8%, respectively. After

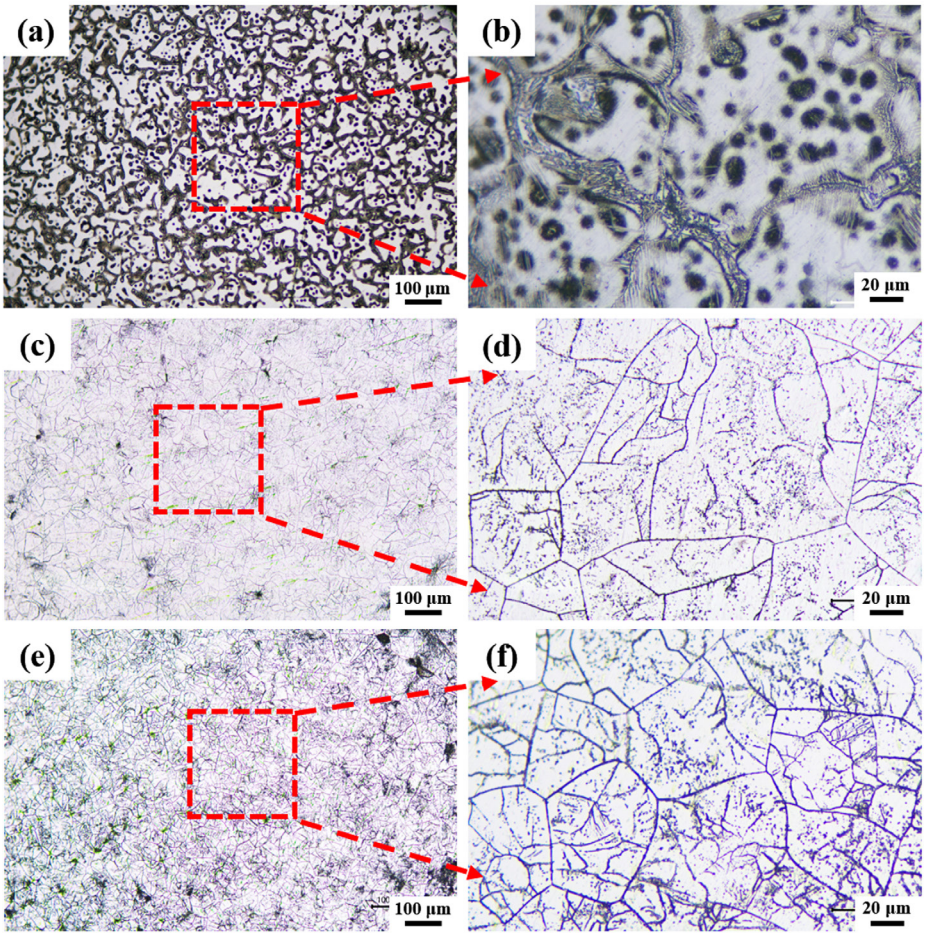

Fig. 2: OM images of $Ti_{35}Zr_{25}Ta_{15}Nb_{15}Sn_{10}$ BHEAs after solidification at different pressures: (a, b) 0.1 MPa; (c, d) 4 GPa; (e, f) 7 GPa

solidification at 4 GPa, a large number of nanoprecipitated phases are found in the matrix, and they are unevenly distributed and gather near the subgrain boundary, as shown in Figs. 3(c) and (d). Similarly, after solidification at 7 GPa, $Ti_{35}Zr_{25}Ta_{15}Nb_{15}Sn_{10}$ BHEA also has nanoprecipitation near the subgrain boundary. Compared with 4 GPa, the precipitated phase increases in size and tends to form regular spheres, as shown in Figs. 3(e) and (f). The average sizes of the precipitated phase can be calculated by nano-measure software, which are 0.61 μm and 0.66 μm at pressures of 4 GPa and 7 GPa, respectively, as shown in Fig. 4.

To determine the compositions of the $Ti_{35}Zr_{25}Ta_{15}Nb_{15}Sn_{10}$ BHEAs after solidification at different pressures, the element distributions of the alloys were scanned (Fig. 5). At ambient pressure, Nb is relatively uniform, Ti and Ta are mainly distributed in the matrix, and Zr and Sn are mainly distributed in the needle-like phase. When solidified at 4 GPa, Ti, Zr, Nb and Ta are uniformly distributed, while Sn mainly exists in the nanoprecipitated phase in the matrix and grain boundary, and a precipitate-free zone (PFZ) is formed at the grain boundary. The element distribution at 7 GPa is almost the same as that at 4 GPa.

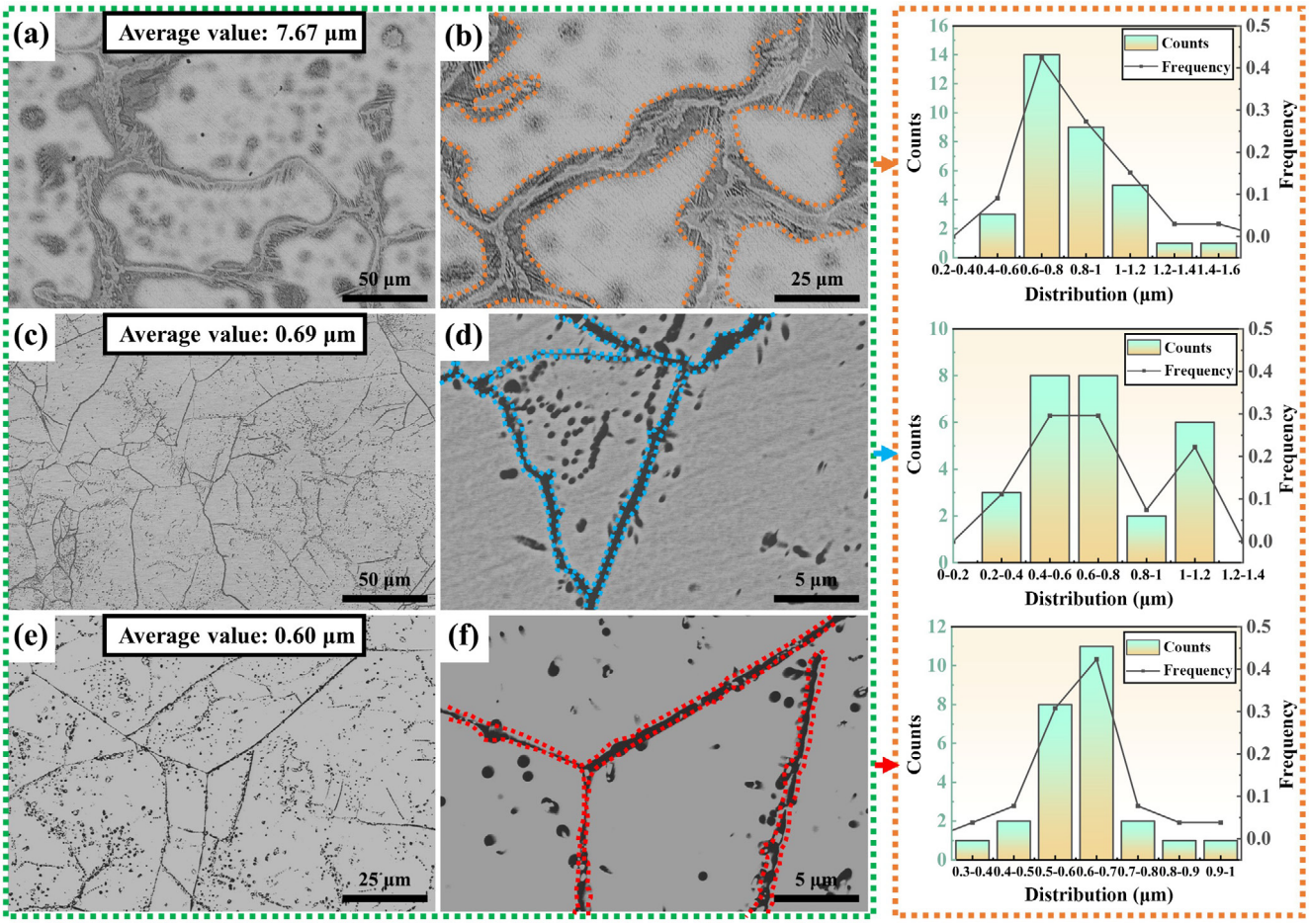

Fig. 3: Backscattered electron (BSE) morphology and grain boundary spacing characteristics of $Ti_{35}Zr_{25}Ta_{15}Nb_{15}Sn_{10}$ BHEAs after solidification at different pressures: (a, b) 0.1 MPa; (c, d) 4 GPa; (e, f) 7 GPa

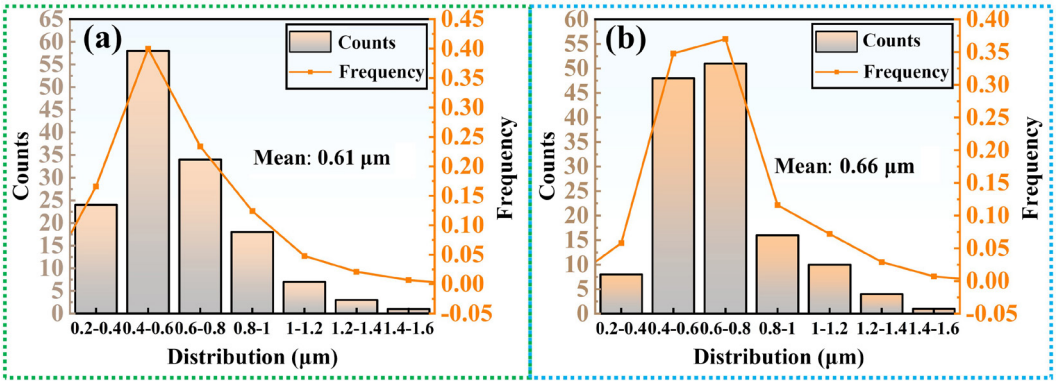

Fig. 4: Average sizes of precipitated phases in matrix of $Ti_{35}Zr_{25}Ta_{15}Nb_{15}Sn_{10}$ BHEAs at high pressures: (a) 4 GPa; (b) 7 GPa

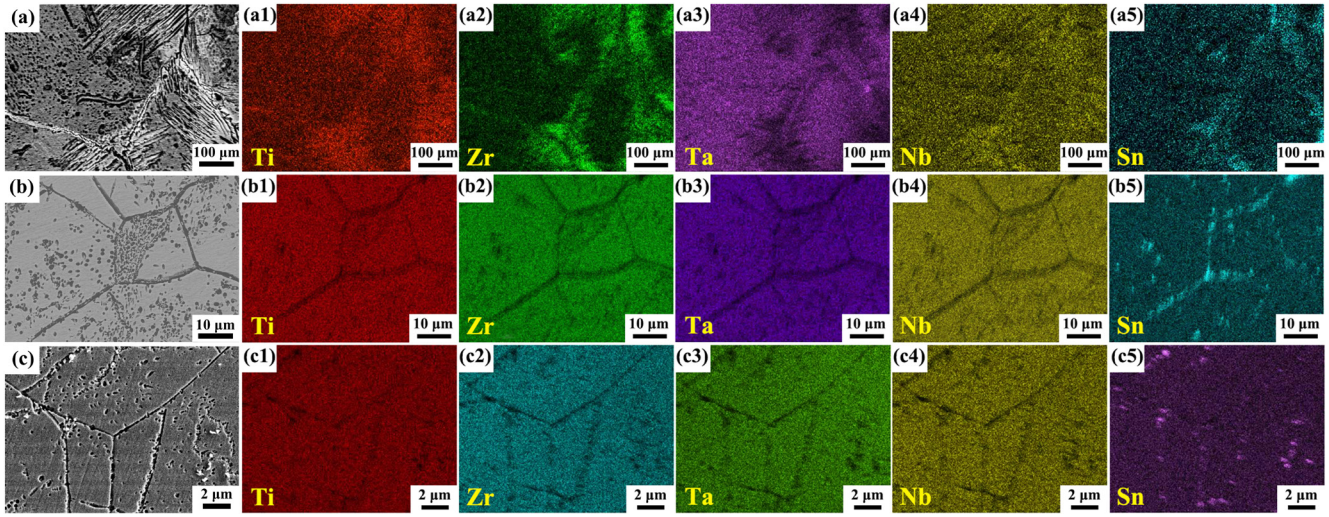

Fig. 5: Mapping scanning results of $Ti_{35}Zr_{25}Ta_{15}Nb_{15}Sn_{10}$ BHEAs after solidification at different pressures: (a–a5) 0.1 MPa; (b–b5) 4 GPa; (c–c5) 7 GPa

The phase constitution of each alloy was analyzed by XRD, the results are shown in Fig. 6. Obviously, the phase constitution is not changed at high pressure, and still is composed of BCC+HCP phase. However, the peak of the HCP phase is found only at 32.1° and 35.98° at ambient pressure, while it is found at 31.96°, 35.83° and 39.73° at 4 GPa and 31.94°, 35.69° and 39.62° at 7 GPa, respectively. The diffraction peak at the same position shifts to a low phase angle with increasing the solidification pressure. Combined with the Bragg equation, it can be inferred that the value of crystal plane spacing d increases.

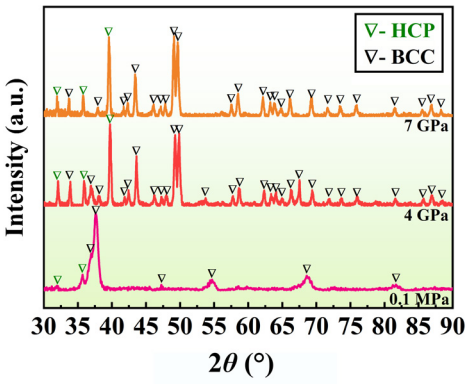

Fig. 6: X-ray diffraction patterns of $Ti_{35}Zr_{25}Ta_{15}Nb_{15}Sn_{10}$ BHEAs prepared at different pressures

The crystal structures of the matrix, needle-like phase and nanoprecipitated phase of the alloy prepared at ambient pressure and 4 GPa are further determined by TEM and HRTEM analysis. The TEM images of $Ti_{35}Zr_{25}Ta_{15}Nb_{15}Sn_{10}$ BHEA after solidification at ambient pressure are presented in Fig. 7. The thickness of the needle-like phase is 120.5 nm [Fig. 7(a)]. The corresponding HRTEM is shown in Figs. 7(b)–(d). The Fourier transform (FFT) [Fig. 7(d)] corresponds to the SAED pattern along the [01$\bar{1}$1] zone axis of the HCP structure

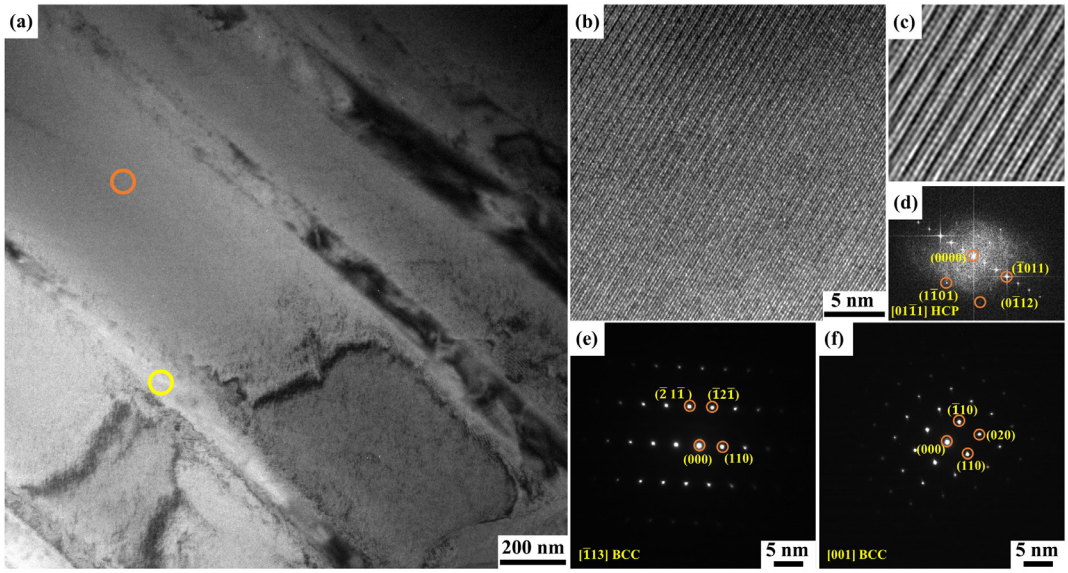

Fig. 7: TEM images of $Ti_{35}Zr_{25}Ta_{15}Nb_{15}Sn_{10}$ BHEAs after solidification at 0.1 MPa: (a) BF-TEM image; (b) HRTEM image showing the needle-like phase (yellow circle); (c) inverse Fourier transform images; (d) Fourier transform images; (e) and (f) SAED for matrix

with two weak spots evenly distributed between two bright points. The inverse Fourier transform (IFFT) [Fig. 7(c)] shows two different sizes of atoms with strong contrast and a small atom with weak contrast. This proves that the needle-like phase has a long-range order structure and the crystal lattice follows the stacking order of ABCABCABC…. Therefore, the needle-like phase represents the HCP Zr_5Sn_3 intermetallic compound. The SAED with zone axis [$\bar{1}$13] [Fig. 7(e)] and [001] [Fig. 7(f)] proves that the matrix possesses a disordered BCC structure.

To further study the microstructure of the nanoprecipitation and its relationship with the matrix, the TEM image of the $Ti_{35}Zr_{25}Ta_{15}Nb_{15}Sn_{10}$ BHEA after solidification at 4 GPa is presented in Fig. 8. BF-TEM shows that the precipitates are not all spherical [Fig. 8(a)], and the insets are the HRTEM micrographs of the interface between the BCC-matrix and HCP-precipitation. The corresponding FFT and IFFT images are shown in Figs. 8(c) and (d). The orientation relationship between the BCC and HCP can be determined from the diffraction patterns viewed along the $[\bar{1}11]_{BCC}$ // $[2\bar{1}\bar{1}0]_{HCP}$ in Fig. 8(c). IFFT conforms to the characteristics of an incoherent interface [Fig. 8(d)]. The DF-TEM images of the matrix prove that plate-shaped nanoprecipitates are generated in the matrix [Fig. 8(e)]. Figures 8(f)–(h) show the HRTEM, FFT and IFFT of the area where contains long range ordered phase (LRO). IFFT [Fig. 8(g)] and FFT [Fig. 8(h)] are performed on the square area in Fig. 8(f), where the superlattice structure is generated. The diffraction spots with the zone axis [$\bar{1}$11] [Fig. 8(h)] and the atomic distribution [Fig. 8(g)] indicate that two atomic planes with weak contrast are distributed between two atomic planes with strong contrast.

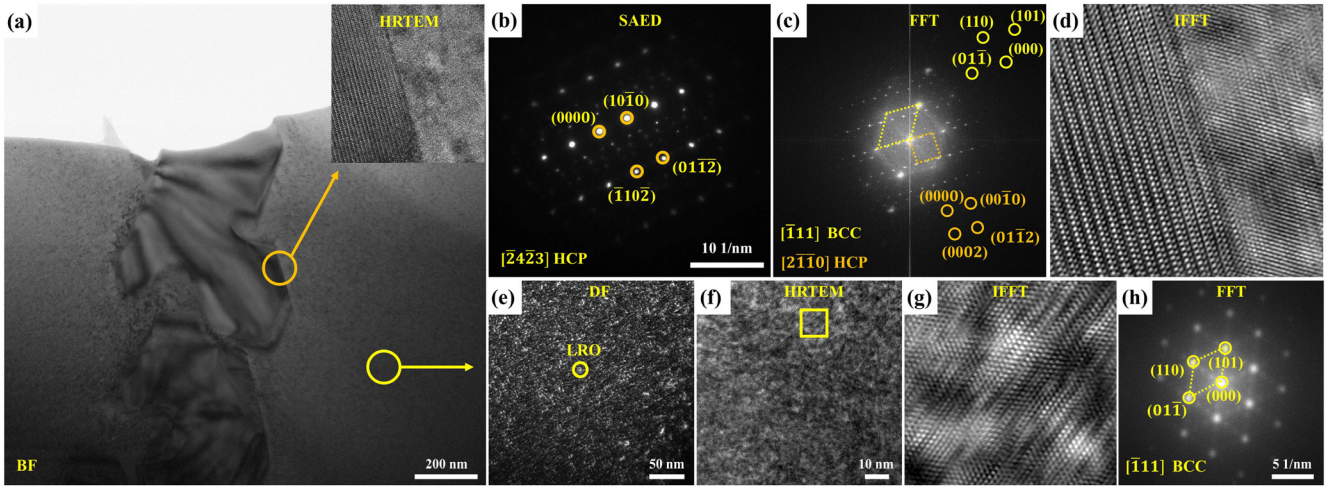

Fig. 8: TEM images of $Ti_{35}Zr_{25}Ta_{15}Nb_{15}Sn_{10}$ BHEAs solidified at 4GPa: (a) BF-TEM image; (b) SAED of nanoprecipitation; (c) Fourier transform images at interface; (d) inverse Fourier transform images; (e) DF image of matrix; (f)–(h) HRTEM image showing the matrix (orange circle)

3.2 Corrosion property characterization

Figure 9 shows the potentiodynamic polarization curves of the $Ti_{35}Zr_{25}Ta_{15}Nb_{15}Sn_{10}$ BHEAs prepared at different pressures in 3.5wt.% NaCl solution. Obviously, the curves of the three alloys are similar, indicating that the alloys have similar redox reactions. In the anode region, the curve is firstly characterized by active dissolution, followed by a rapid decline in the corrosion current density, which is explained by the formation of a corrosion product layer slowing the electrode reaction process [40, 41]. The key parameters derived by the Tafel extrapolation method, such as the corrosion current density (I_{corr}) and the corrosion potential (E_0), are listed in Fig. 10 and Table 1, respectively. Notably, I_{corr} decreases with the increasing pressure, and the values at 4 GPa and 7 GPa are 2.47×10^{-7} A·cm^{-2} and 1.65×10^{-7} A·cm^{-2}, respectively. The value of I_{corr} at 7 GPa is lower than that of the alloy at ambient pressure by approximately 44.5%, which can be considered a significant improvement of corrosion resistance. E_0 reflects the thermodynamics of the material and the surface state of the electrode. When the value of E_0 is negative, the lower the value is, the higher the corrosion

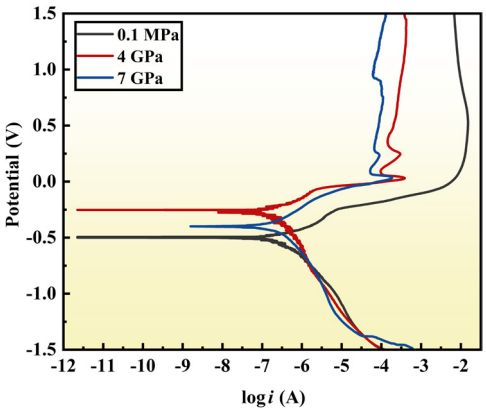

Fig. 9: Polarization curves for $Ti_{35}Zr_{25}Ta_{15}Nb_{15}Sn_{10}$ BHEA at different pressures

tendency. Obviously, the values at 4 GPa and 7 GPa are –0.27 V and –0.40 V, respectively, which are greater than that at the ambient pressure, indicating that the thermodynamic conditions for self-corrosion of the alloy prepared at high pressure are relatively high, self-corrosion is relatively difficult to occur.

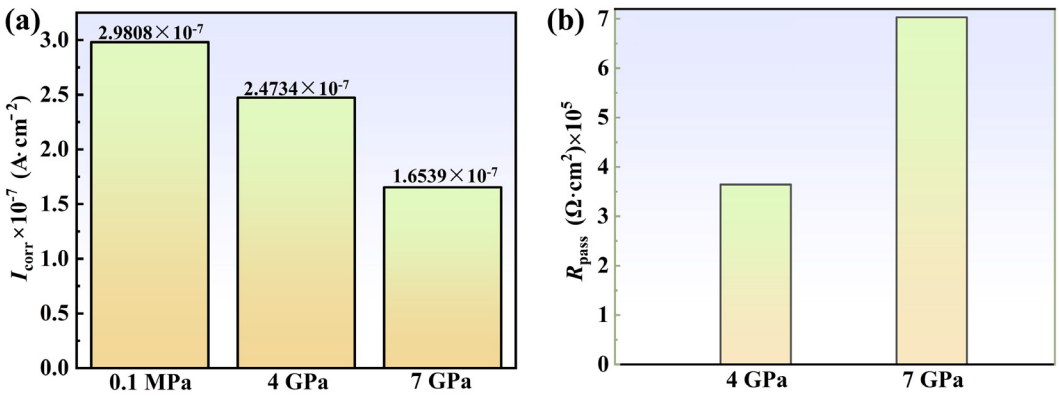

Fig. 10: Corrosion resistance of $Ti_{35}Zr_{25}Ta_{15}Nb_{15}Sn_{10}$ BHEA after solidification at different pressures: (a) I_{corr}; (b) R_{pass}

Table 1: Key electrochemical parameters of $Ti_{35}Zr_{25}Ta_{15}Nb_{15}Sn_{10}$ HEAs at different pressures

Pressure	E_0 (V)	β_a	β_c
0.1 MPa	−0.5000	0.13891	0.34791
4 GPa	−0.2666	0.09729	0.14906
7 GPa	−0.4004	0.19611	0.25110

Figure 11 shows the impedance spectroscopy of the $Ti_{35}Zr_{25}Ta_{15}Nb_{15}Sn_{10}$ BHEAs solidified at different pressures. Clearly, the radius of the impedance arc increases with increasing the solidification pressure [Fig. 11(a)]. For the sample prepared at 0.1 MPa, the end of the capacitive reactance arc in the Nyquist curve, corresponding to the low frequency region, presents an oblique line, which suggests the possible presence of Warburg impedance, suggesting that the polarization progress is controlled by ion diffusion. In the Bode diagram, the peak of the frequency-phase angle curve in the frequency range of 10–10^3 Hz shows a widening trend, which means that there are two time constants in the electrochemical system. The Nyquist curve fitted by the equivalent circuit models coincides well with the experimental results [Fig. 11(b)], which proves that the established equivalent circuit diagram [Fig. 11(c)] can effectively explain the corrosion behaviors of the $Ti_{35}Zr_{25}Ta_{15}Nb_{15}Sn_{10}$ BHEAs prepared at different pressures. The Bode plots in Fig. 11(d) show the phase angles of samples prepared at ambient pressure and 4 GPa are close to 70°, while the phase angle at 7 GPa is approximately 80° in a wide frequency range. It can be proven that the corrosion product layer at 7 GPa has a stronger corrosion resistance and protective effect. Considering that the actual capacitance characteristics of the corrosion product layer are not completely consistent with the theoretical capacitance, the

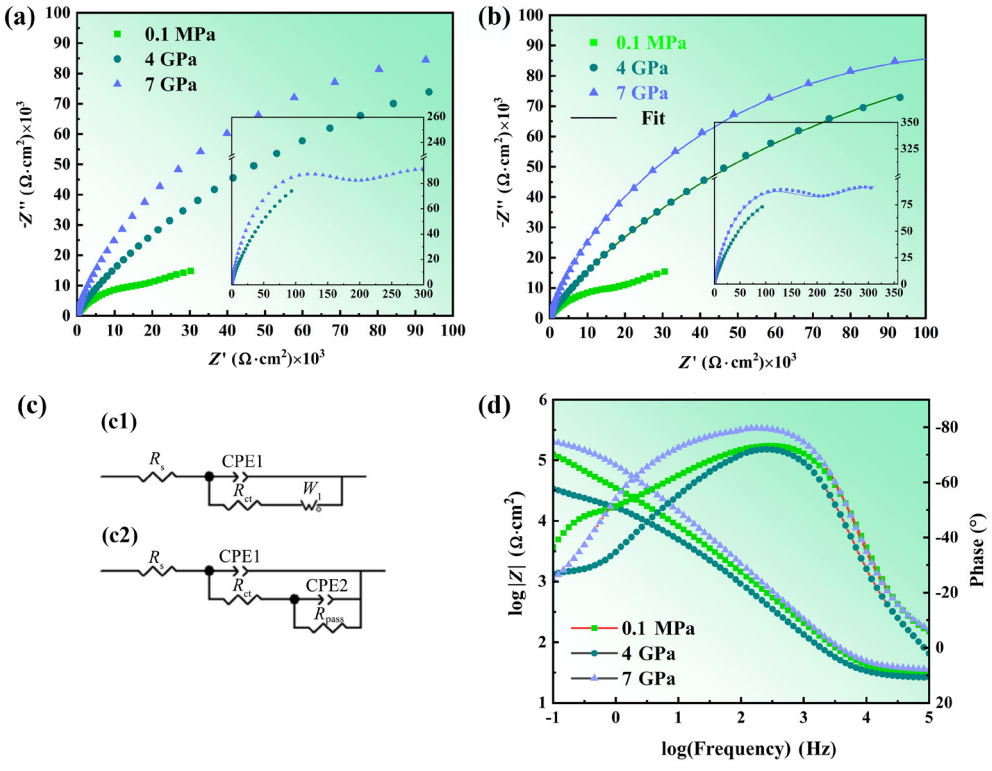

Fig. 11: EIS images of $Ti_{35}Zr_{25}Ta_{15}Nb_{15}Sn_{10}$ BHEAs after solidification at different pressures: (a) Nyquist plots; (b) fitting results; (c) EIS spectrum equivalent circuit; (d) Bode plots

constant-phase elements (CPEs) were selected to replace the ideal capacitance [42, 43]. R_s represents the solution resistance. The parallel connection of CPE1 and R_{ct} is used to indicate the properties of the double electric layer. In the case of 0.1 MPa, W_1 represents the ion diffusion resistance. CPE2 and R_{pass} are connected in parallel to represent the charge transfer process of the corrosion product layer.

The fitting results of different parameters in the equivalent circuit model are listed in Table 2. It can be seen from Table 2 that R_{ct} values at different pressures are 1,629 Ω·cm^2, 4,156 Ω·cm^2, and 14,362 Ω·cm^2, respectively. The R_{pass} values at 4 GPa and 7 GPa are 3.64×10^5 and 7.03×10^5 Ω·cm^2, respectively, as shown in Fig. 10(b). This phenomenon shows that the charge transfer between the double layers is becoming increasingly difficult. This finding suggests that with increasing solidification pressure, the density and protection of corrosion product films are significantly improved.

The corrosion surface morphology is observed by SEM, as shown in Fig. 12. The selective corrosion occurs at the grain boundaries of the alloys prepared under the three conditions. The ambient pressure sample is the most seriously corroded, and the needle-like HCP-Zr_5Sn_3 at the grain boundaries is completely corroded. In addition, the matrix of the three alloys all has different degrees of uniform corrosion. Obviously, the degree of general corrosion of the alloy matrix decreases with increase of solidification pressure. This finding indicates that the corrosion products formed in the microstructures solidified under high pressures are more likely to form a dense protective layer, greatly enhancing the corrosion resistance of the alloy.

Table 2: Fitting values of equivalent circuits of $Ti_{35}Zr_{25}Ta_{15}Nb_{15}Sn_{10}$ BHEAs after solidification at different pressures

Pressure	R_s (Ω·cm^2)	CPE1-T (μF·cm^{-2})	CPE1-P	R_{ct} (Ω·cm^2)	CPE2-T (μF·cm^{-2})	CPE2-P	R_{pass} (Ω·cm^2)	W_1 (Ω·cm^2)
0.1 MPa	29.6	3.32E-06	0.88	1,629	–	–	–	110,840
4 GPa	30.2	1.79E-06	0.91	4,156	7.28E-06	0.54	364,300	–
7 GPa	35.6	1.01E-0.6	0.92	14,362	3.45E-06	0.55	703,000	–

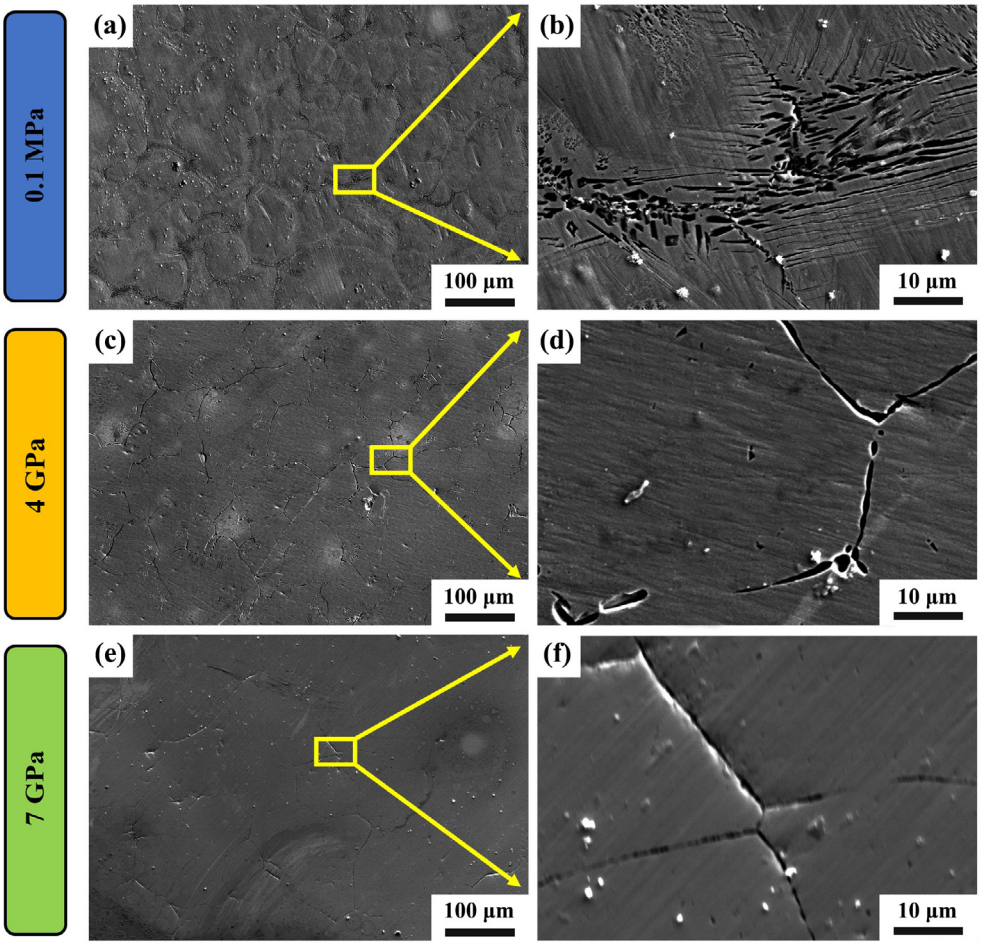

Fig. 12: Corrosion morphologies of $Ti_{35}Zr_{25}Ta_{15}Nb_{15}Sn_{10}$ BHEA after solidification at different pressures: (a, b) 0.1 MPa; (c, d) 4 GPa; (e, f) 7 GPa

4 Discussion

The primary (Ti, Nb, Ta)-rich phase preferentially nucleates and grows at the initial stage of the solidification of the $Ti_{35}Zr_{25}Ta_{15}Nb_{15}Sn_{10}$ BHEA at ambient pressure. During the continuous growth process, Zr and Sn atoms are constantly discharged from the front of the solid-liquid interface [44]. Therefore, in the final stage of solidification, a large number of Zr and Sn atoms existed in the remaining liquid phase transform into a supersaturated solid solution. As the temperature decreases, Zr and Sn atoms diffuse and aggregate at grain boundaries, precipitating in the form of needle like phases, and finally forming the Zr_5Sn_3 phase. When the $Ti_{35}Zr_{25}Ta_{15}Nb_{15}Sn_{10}$ BHEA solidifies at an ultra-high pressure, the solid solubility of Zr and Sn atoms in the primary (Ti, Nb, Ta)-rich phase can be greatly improved, forming a large saturated solid solution. Continuing cooling after alloy solidification will results in uniform dispersion and precipitation of (Zr, Sn)-rich nanoparticles in the matrix ((Ti, Nb, Ta)-rich phase), or the formation of heterogeneous structures (Fig. 8).

Based on Figs. 12(a) and (b), it can be seen that at ambient pressure corrosion mainly occurs at grain boundaries and needle-like Zr_5Sn_3 phases that grow parallel to the grain boundaries. Narrow bands with relatively poor concentrations of Zr and Sn elements and enriched with Nb, Ti, and Ta elements appear near the Zr_5Sn_3 phase (Fig. 13). Thus, the corrosion product layer is relatively weak, which facilitates the intrusion of Cl ions into the electrode surface. A microbattery is formed between the Zr_5Sn_3 phase and the matrix, and due to the lowest electrochemical potential at the boundary, the Zr_5Sn_3 phase is preferentially dissolved as an anode during the corrosion process. After $Ti_{35}Zr_{25}Ta_{15}Nb_{15}Sn_{10}$ BHEA solidification at a high pressure, the sample mainly experiences pitting corrosion and grain boundary corrosion. Based on Fig. 5, it can be seen that at high pressure conditions, Sn is distributed in the precipitated phase within the crystal. Figures 12(c)–(f) show that pitting corrosion preferentially occurs in areas enriched with Sn. Research has shown that the electrode potential of each element in $Ti_{35}Zr_{25}Ta_{15}Nb_{15}Sn_{10}$ BHEA is: $\varphi_{Sn}<\varphi_{Ta}<\varphi_{Nb}<\varphi_{Zr}<\varphi_{Ti}$ [45]. The alloys prepared under the three conditions all experience grain boundary corrosion. Due to the high energy of grain boundaries, edge dislocations and vacancies are concentrated at grain boundaries, and the electrochemistry of grains and grain boundaries is inhomogeneous, making grain boundaries more susceptible to corrosion [46]. Therefore, the corrosion resistance of the alloy is closely related to the width of the grain boundary. Although obvious grain boundaries exist in the alloy, according to Figs. 3 and 12, it can be seen that the grain boundaries of the alloy prepared under high-pressure conditions are narrow, and the potential difference within the matrix is reduced, improving the corrosion resistance of the alloy.

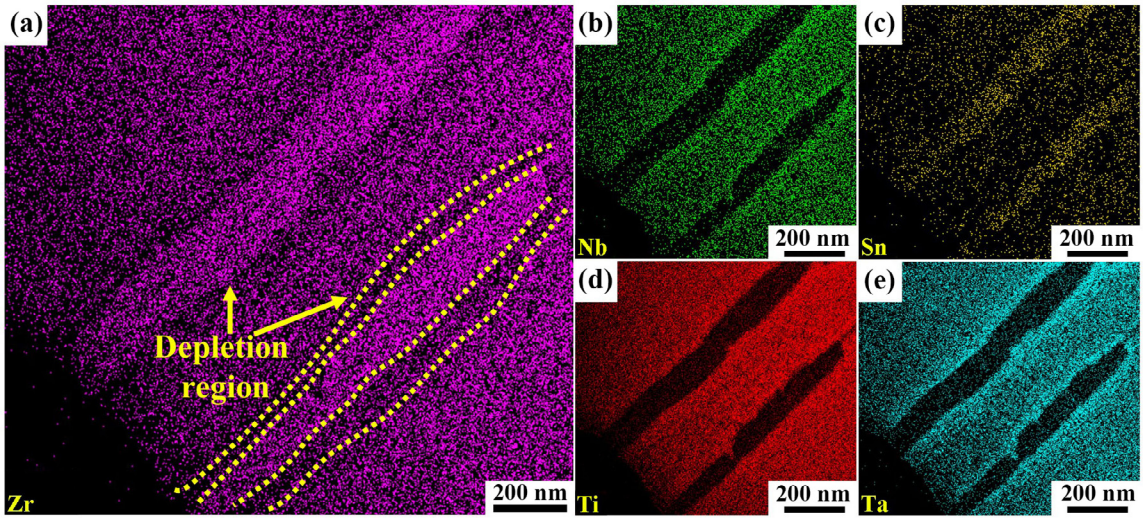

Fig. 13: Map scanning results of $Ti_{35}Zr_{25}Ta_{15}Nb_{15}Sn_{10}$ BHEA after solidification at ambient pressure (a–e)

5 Conclusions

The microstructure evolution, phase constitution, and electrochemical corrosion properties of the $Ti_{35}Zr_{25}Ta_{15}Nb_{15}Sn_{10}$ BHEAs after solidification at different pressures were studied. According to the obtained results and analysis, the main conclusions can be summarized as follows:

(1) At ambient pressure, the microstructure of the $Ti_{35}Zr_{25}Ta_{15}Nb_{15}Sn_{10}$ BHEA consists of a BCC matrix and needle-like Zr_5Sn_3 phases growing parallel to the matrix. After solidification at high pressure, the needle-like phase disappears.

(2) A large number of nanoprecipitated phases [(Zr, Sn)-rich] are found in the matrix after solidifiation at high pressures. The orientation relationship between the BCC (matrix) and HCP (nanophase) can be determined to be $[\bar{1}11]_{BCC}$ // $[2\bar{1}\bar{1}0]_{HCP}$.

(3) The interdendritic spacing is approximately 7.67 μm when solidified at ambient pressure. After solidification at 4 GPa and 7 GPa, it decreases by 91% and 92.8%, respectively.

(4) The orrosion current density I_{corr} decreases with an increase in pressure, and the values decrease from 2.98×10^{-7} A·cm^{-2} at ambient pressure to 1.65×10^{-7} A·cm^{-2} at 7 GPa.

Acknowledgments

This work was financially supported by the Natural Science Foundation of Zhejiang Province (No. LZY23E050001) and the National Natural Science Foundation of China (Nos. 52271106, 52171120, 52001262).

Conflict of interest

The authors declare that they have no conflict of interest.

References

[1] Makurat-Kasprolewicz B, Ossowska A. Recent advances in electrochemically surface treated titanium and its alloys for biomedical applications: A review of anodic and plasma electrolytic oxidation methods. Materials Today Communications, 2023, 34: 105425.
[2] Chouirfa H, Bouloussa H, Migonney V, et al. Review of titanium surface modification techniques and coatings for antibacterial applications. Acta Biomaterialia, 2019, 83: 37–54.
[3] Zhu Z, Liu Y, Chen Z, et al. High-strength Ti-Al-V-Zr cast alloys designed using α and β cluster formulas. China Foundry, 2023, 20(1): 23–28.
[4] Sahoo P, Das S K, Paulo Davim J. Tribology of materials for biomedical applications. Vol. 1, ed. Paulo Davim J, Mechanical Behaviour of Biomaterials, 2019: 1–45.
[5] Tsutsumi Y, Niinomi M, Nakai M, et al. Micro-arc oxidation treatment to improve the hard-tissue compatibility of Ti-29Nb-13Ta-4.6Zr alloy. Applied Surface Science, 2012, 262: 34–38.
[6] Costa N A, Correa D R N, Lisboa-Filho P N, et al. Influence of the molybdenum on characteristics of oxide films produced by micro-arc oxidation on Ti-15Zr-based alloys. Surface and Coatings Technology, 2021, 408: 126856.
[7] Xu Y F, Liu H Q, Zhang S, et al. Effect of duplex aging on microstructural and mechanical behavior of a new β-Ti alloy for biomedical applications. Journal of Materials Research and Technology, 2022, 18: 2870–2884.
[8] Ozaltin K, Chrominski W, Kulczyk M, et al. Enhancement of mechanical properties of biocompatible Ti-45Nb alloy by hydrostatic extrusion. Journal of Materials Science, 2014, 49: 6930–6936.
[9] Sarabjeet S S, Harpreet S, Mohamed A G. A review on alloy design, biological response, and strengthening of β-titanium alloys as biomaterials. Materials Science and Engineering: C, 2021, 121: 111661.
[10] Gouda M K, Gepreel M A H, Yamanaka K, et al. Chiba cold-workability and microstructure change with β-phase stability in high-strength Ti-Mn binary alloys. JOM, 2019, 71(10): 3590–3599.
[11] Sadeghpour S, Abbasi S M, Morakabati M. Design of a new multi-element beta titanium alloy based on d-electron method. In: 147th Annual Meeting & Exhibition Supplemental Proceedings, The Minerals, Metals and Materials Series, 2018: 377–386.
[12] Min X H, Emura S, Nishimura T, et al. Microstructure, tensile deformation mode and crevice corrosion resistance in Ti-10Mo-*x*Fe alloys. Materials Science and Engineering: A, 2010, 527(21–22): 5499–5506.
[13] Ozan S, Lin J, Weng W, et al. Bioactive materials effect of thermomechanical treatment on the mechanical and microstructural evolution of a β-type Ti-40.7Zr-24.8Nb alloy. Bioactive Materials, 2019, 4: 303–311.
[14] Li T X, Miao J W, Lu Y P, et al. Effect of Zr on the as-cast microstructure and mechanical properties of lightweight $Ti_2VNbMoZr_x$ refractory high-entropy alloys. International Journal of Refractory Metals and Hard Materials, 2022, 103: 105762.
[15] Loffler T, Ludwig A, Rossmeisl J, et al. What makes high-entropy alloys exceptional electrocatalysts. Angewandte Chemie International, 2021, 60(52): 26894–26903.
[16] Ma X, Hu Y, Wang K, et al. Microstructure and mechanical properties of a low activation cast WTaHfTiZr refractory high-entropy alloy. China Foundry, 2022, 19(6): 489–494.
[17] Guo Q W, Pan Y, Hou H, et al. Predicting the hardness of high-entropy alloys based on compositions. International Journal of Refractory Metals and Hard Materials, 2023, 112: 106116.
[18] Rosenkranz L, Feuerbacher M, Gadelmeier C, et al. Tensile behavior of hexagonal rare-earth-based low, medium, and high entropy alloys: Strengthening effect of configurational entropy. Intermetallics, 2023, 155: 107835.
[19] Liu P, Xiang H, Li H, et al. Enhancement mechanism of fracture-resistance of CrMnFeCoNi high-entropy alloys: A molecular dynamics study. Advanced Powder Technology, 2022, 33: 103603.
[20] Xu L, Jia Y, Wang Z, et al. Dual precipitate simultaneous enhancement of tensile and fatigue strength in $(FeCoNi)_{86}Al_7Ti_7$ high-entropy alloy fabricated using selective laser melting. Journal of Materials Science & Technology, 2023, 148: 90–104.
[21] Yang J, Feng D, Liu Y, et al. Excellent corrosion resistance of electron beam welded joint and remelted layer of eutectic high-entropy alloy AlCoCrFeNi2.1. Intermetallics, 2023, 154: 107822.
[22] Dewangan S K, Kumar D, Sharma A, et al. Enhancing the oxidation resistance of nanocrystalline high-entropy AlCuCrFeMn alloys by the addition of tungsten. Journal of Materials Research and Technology, 2022, 21: 4960–4968.
[23] Li T X, Wang S D, Fan W X, et al. CALPHAD-aided design for superior thermal stability and mechanical behavior in a TiZrHfNb refractory high-entropy alloy. Acta Materialia, 2023, 246: 118728.
[24] Li T X, Lu Y P, Li Z Q, et al. Hot deformation behavior and microstructure evolution of non-equimolar $Ti_2ZrHfV_{0.5}Ta_{0.2}$ refractory high-entropy alloy. Intermetallics, 2022, 146: 107586.
[25] Wu Y D, Cai Y H, Wang T, et al. A refractory $Hf_{25}Nb_{25}Ti_{25}Zr_{25}$ high-entropy alloy with excellent structural stability and tensile properties. Materials Letters, 2014, 130: 277–280.
[26] Todai M, Nagase T, Hori T, et al. Novel TiNbTaZrMo high-entropy alloys for metallic biomaterials. Scripta Materialia, 2017, 129: 65–68.
[27] Wang S P, Xu J. TiZrNbTaMo high-entropy alloy designed for orthopedic implants: As-cast microstructure and mechanical properties. Materials Science and Engineering: C, 2017, 73: 80–89.
[28] Motallebzadeh A, Peighambardoust N S, Sheikh S, et al. Microstructural, mechanical and electrochemical characterization of TiZrTaHfNb and $Ti_{1.5}ZrTa_{0.5}Hf_{0.5}Nb_{0.5}$ refractory high-entropy alloys for biomedical applications. Intermetallics, 2019, 113: 106572.
[29] Shi Y, Yang B, Liaw P K. Corrosion-resistant high-entropy alloys: A review. Metals, 2017, 7(2): 43.
[30] Yang W, Liu Y, Pang S, et al. Bio-corrosion behavior and in vitro biocompatibility of equimolar TiZrHfNbTa high-entropy alloy. Intermetallics, 2020, 124: 106845.
[31] Zhou Q, Sheikh S, Ou P, et al. Corrosion behavior of $Hf_{0.5}Nb_{0.5}Ta_{0.5}Ti_{1.5}Zr$ refractory high-entropy in aqueous chloride solutions. Electrochemistry Communications, 2019, 98: 63–68.

[32] Wang Z, Yan Y, Wu Y, et al. Corrosion and tribocorrosion behavior of equiatomic refractory medium entropy TiZr(Hf, Ta, Nb) alloys in chloride solutions. Corrosion Science, 2022, 199: 110166.
[33] Zhao C, Pan F, Zhao S, et al. Preparation and characterization of as-extruded Mg-Sn alloys for orthopedic applications. Materials & Design, 2015, 70: 60–67.
[34] Chen J H, Chhetri T P, Grant A T, et al. The effects of Cu-substitution and high-pressure synthesis on phase transitions in Ni_2MnGa Heusler alloys. Journal of Alloys and Compounds, 2022, 900: 163480.
[35] Chang T, Zou C M, Zhu D D, et al. The evolution of microstructure, micromechanical and magnetic properties of FeCoNiAlSi alloys with peritectic structure processed by high-pressure solidification. Journal of Alloys and Compounds, 2022, 920: 165958.
[36] Tong X, Cai W, Lin J, et al. Biodegradable Zn-3Mg-0.7Mg_2Si composite fabricated by high-pressure solidification for bone implant applications. Acta Biomaterialia, 2021, 123: 407–417.
[37] Lin X, Dai P, Xu C, et al. Solute redistribution and mechanism of structure refinement of Mg-Al alloy during solidification under high pressure. Journal of Alloys and Compounds, 2022, 910: 164777.
[38] Liu X, Ma P, Jia Y D, et al. Solidification of Al-*x*Cu alloy under high pressures. Journal of Materials Research and Technology, 2020, 9: 2983–2991.
[39] Lin X, Kuo Y, Wang L, et al. Refinement and strengthening mechanism of Mg-Zn-Cu-Zr-Ca alloy solidified under extremely high pressure. Transactions of Nonferrous Metals Society of China, 2021, 31: 1587–1598.
[40] Lv Y T, Lang X W, Zhang Q, et al. Study on corrosion behavior of (CuZnMnNi)(100−*x*)Sn-*x* high-entropy brass alloy in 5 wt% NaCl solution. Journal of Alloys and Compounds, 2022, 921: 166051.
[41] Wu L, Xu Y T, Ma A L, et al. Influence of pre-immersion aeration conditions on corrosion product films and erosion-corrosion resistance of 90/10 and 70/30 copper-nickel tubes in 1wt% NaCl solution. Corrosion Science, 2024, 228: 111817.
[42] Brug G J, Van Den Eeden A L G, Sluyters-Rehbach M, et al. The analysis of electrode impedances complicated by the presence of a constant phase element. Journal of Electroanalytical Chemistry and Interfacial Electrochemistry, 1984, 176(1): 275–295.
[43] Macdonald J R. Impedance spectroscopy. Annals of Biomedical Engineering, 1992, 20(3): 289–305.
[44] Sobczak J J, Drenchev L, Asthana R. Effect of pressure on solidification of metallic materials. International Journal of Cast Metals Research, 2012, 25(1): 1–14.
[45] David R. CRC handbook of chemistry and physics. Journal of the American Chemical Society, 2007, 129(3): 724–724.
[46] Mondou E, Proietti A, Charvillat C, et al. Understanding the mechanisms of intergranular corrosion in 2024 Al alloy at the polycrystal scale. Corrosion Science, 2023, 221: 111338.